Inorganic Chemistry

pubs.acs.org/IC

Article

Engineering of the *XY* Magnetic Layered System with Adeninium Cations: Monocrystalline Angle-Resolved Studies of Nonlinear Magnetic Susceptibility

Emilia Kuzniak-Glanowska, Piotr Konieczny,* Robert Pełka, Tadeusz M. Muzioł, Marcin Kozieł, and Robert Podgajny*

Cite This: *Inorg. Chem.* 2021, 60, 10186−10198

Read Online

ACCESS | Metrics & More | Article Recommendations | Supporting Information

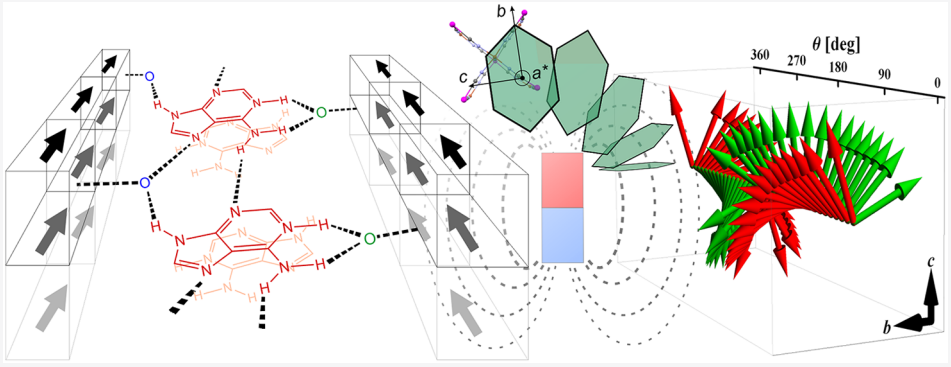

ABSTRACT: An original example of *modular* crystal engineering involving molecular magnetic $\{Cu^{II}[W^{V}(CN)_8]\}^-$ bilayers and adeninium cations ($AdeH^+$) toward the new layered molecular magnet $(AdeH)\{Cu^{II}[W^{V}(CN)_8]\}\cdot 2H_2O$ (**1**) is presented. **1** crystallizes within the monoclinic *C*2 space group (a = 41.3174(12), b = 7.0727(3), c = 7.3180(2) Å, β = 93.119(3)°, and V = 2135 Å^3). The bilayer topology is based on a stereochemical matching between the square pyramidal shape of Cu^{II} moiety and the bicapped trigonal prismatic shape of $[W^{V}(\mu\text{-}CN)_5(CN)_3]$, and the separation between bilayers is significantly increased (by ∼50%; from ca. 9.5 to ca. 14.5 Å) compared to several former analogues in this family. This was achieved via a unique combination of (i) a 1D ribbonlike hydrogen bond system $\{AdeH^+\cdots H_2O\cdots AdeH^+\cdots\}_\infty$ exploiting planar water-assisted Hoogsteen···Sugar synthons with (ii) parallel 1D $\pi-\pi$ stacks $\{AdeH^+\cdots AdeH^+\}_\infty$. In-plane 2D *XY* magnetism is characterized by a T_c close to 33 K, $H_{c,\text{in-plane}}$ = 60 Oe, and $H_{c,\text{out-of-plane}}$ = 750 Oe, high values of in-plane γ critical exponents (γ_b = 2.34(6) for $H \| b$ and γ_c = 2.16(5) for $H \| c$), and a Berezinskii−Kosterlitz−Thouless (BKT) topological phase transition, deduced from crystal-orientation-dependent scaling analysis. The obtained values of in-plane ν critical exponents, ν_b = 0.48(5) for $H \| b$ and ν_c = 0.49(3) for $H \| c$, confirm the BKT transition (ν_{BKT} = 0.5). Full-range angle-resolved monocrystalline magnetic measurements supported by dedicated calculations indicated the occurrence of nonlinear susceptibility performance within the easy plane in a magnetically ordered state. We refer the occurrence of this phenomenon to spontaneous resolution in the *C*2 space group, a tandem not observed in studies on previous analogues and rarely reported in the field of molecular materials. The above *magneto-supramolecular strategy* may provide a novel means for the design of 2D molecular magnetic networks and help to uncover the inherent phenomena.

INTRODUCTION

Layered inorganic materials, e.g., magnetic, conducting, semiconducting, and so on, has gained interest owing to its high potential in construction of spintronic composites, e.g., multilayered spin valves exploiting giant magneto-resistance. In reference to and parallel to the first-choice components toward practical applications (graphene, metals, metalloids, their oxides or chalcogenides, and alloys), modern molecular and coordination chemistry quickly created a parallel extensive research field.[1,2] Very recently, various aspects of formation, flexibility, properties and application perspectives of 2D coordination polymers were very thoroughly reviewed by Vittal and co-workers.[3] Indeed, offering optical transparency, soft matter character, and generally environmentally friendly mild synthesis conditions, layered coordination networks opened a relatively easy access path toward a combination of

Received: February 11, 2021
Published: July 7, 2021

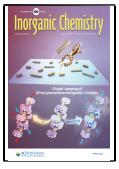

magnetic and optical features, together with their external control.[4] Some layered coordination motifs appear systematically under particular synthesis conditions, and their functionality can be tuned using the variety of accompanying species (anions, cations, and neutral species). Thus, from the viewpoint of crystal engineering, they could be considered secondary building units (SBUs), with structural and functional properties tunable by crystallizing or cocrystallizing agents. Such an approach has been widely employed to achieve a diversity of spin-crossover (SCO) transitions in Hofmann-type $M[M'(CN)_4]$ (M = Fe^{II}; M′ = Ni^{II}, Pd^{II}, and Pt^{II}) clathrates,[5−11] implementation of various additional functions into layered oxalates $\{M[M'(C_2O_4)_3]\}^{0/-}$[12−14] or anilates $\{M[M'(C_6O_4X_2)_3]\}^{-}$[15−18] (M, M′ = divalent or trivalent 3d metal ions), engineering of interlayer separation and long-range magnetic ordering (LRMO) in hybrid layered hydroxides,[19,20] tuning of LRMO in thiocyanato-bridged solid solutions $[Co_xNi_{1-x}(NCS)_2(ligand)_2]_n$,[21] or the very recent electrochemical modification of interlayer nanospace in newly established Cr(pyrazine) family.[22,23] A significant contribution to the field is provided by cyanide-bridged networks with recurrent modular 2D bimetallic backbones MM′·*ligand*·*guest* involving exchangeable $[M'(CN)_8]^{3-/4-}$ (M′ = Mo, W, Re, and Nb) and di- or trivalent 3d metal ions (Mn, Fe, Co, Ni, and Cu), or trivalent 4f ions, M.[24] Various combinations of components did operate within a limited number of topologies to shape LRMO and its anisotropy,[25−27] which was frequently accompanied by externally controlled change in solvate/guest composition,[28,29] charge transfer and spin transition phenomena,[30−34] and charge carrier injection/extraction[35,36] or flow[37,38] phenomena.

Among the above compounds, the anionic $\{M^{II}[M'^{V}(CN)_8]\}^{-}$ (M = Cu and Mn; M′ = Mo and W) bilayers constitute a good example of a systematically recurrent molecular module. The double-decker topological Prussian Blue Analogue (PBA) fragment is achieved due to a stereochemical matching between the square pyramidal (SPY-5) shape of Cu^{II} moiety or octahedral shape of Mn^{II} moiety, and the bicapped trigonal prism (BTRP-8) $[W^{V}(\mu\text{-}CN)_5(CN)_3]$ unit (Figure 1).[39−47] Such double-decker fragments were previously put together by various cationic species: $tetrenH_5^{5+}$ (CuM′),[39] $dienH_3^{3+}$ (CuM′),[40] Cs^+ (CuW, CuMo),[41] guanidinium ($guaH^+$) (CuM′),[42] single Cu^{2+} (CuMo,CuW),[43,44] and Mn^{2+} (MnMo)[45] complexes or polymeric 1D $\{Cu(\mu\text{-}pyz)\}^{2+}$ chains (CuM′).[46] The average interlayer distances varied between ca. 8 and 11 Å, which resulted in LRMO below T_c between 27 and 43 K and coercive field H_c between ca. 2500 Oe and ca. 80 Oe, both parameters decreasing with the increasing interlayer distance in the case of CuM′. The in-plane *XY* magnetism of a single CuW bilayer was recently exploited in the studies of inverse magnetocaloric effect (MCE) and rotational MCE (RMCE),[48] whereas the MnMo bilayers served as platforms for reversible cation (Li^+,Na^+)-electron pairs injections/extractions processes, essential from the viewpoint of the fabrication of lithium batteries.[45]

In this work, we make a step toward crystal engineering of coordination layered magnets using topologically advanced components. This inspiration came from the field of biochemistry: the purine- and pyrimidine-type nucleic bases offer the unique side double or triple hydrogen bond patterns owing to the specific distribution of N-heteroatoms and N−H, C═O, and NH_2 functions.[49−52] Considering the above, and

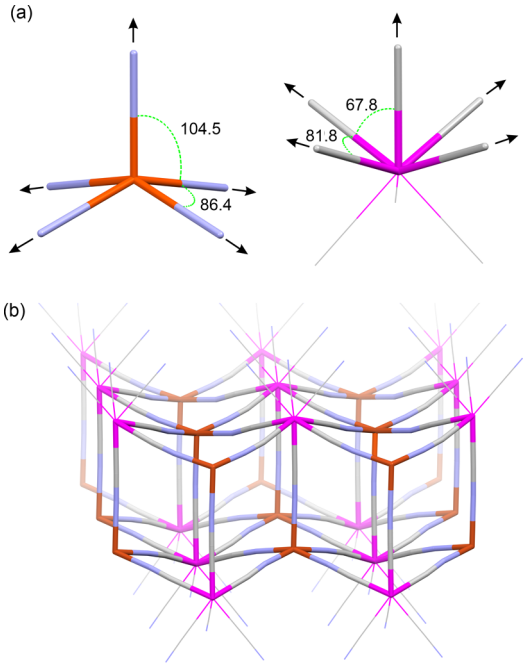

Figure 1. (a) The stereochemistry of the ideal square pyramid (SPY-5) polyhedron (left) almost ideally fits to the distribution of the relevant five out of eight cyanido ligands in a biaugmented trigonal prism polyhedron (representative also for bicapped trigonal prism) (BTRP-8) (right). (b) This allows to us construct the bilayered skeleton in a reproducible manner.[39−42] Some octahedral complexes might adopt this topology with an appropriate fine distortion as well.[43−46] Color and style scheme: pink, W; brick, Cu; pale gray; N, pale blue; sticks: bridging, CN^-; wireframe, terminal CN^-. The arrows show a directionality of cyanido-bridges formation. The angles L−M−L refer to the ideal polyhedra provided within the SHAPE package.[47]

driven also by simple curiosity, we carried out self-assembly tests toward the formation of new solid phases involving $\{Cu^{II}[M^{V}(CN)_8]\}^{-}$, using acidic aqueous solutions as a medium. As a result, we present the crystal structure and complete angle-resolved magnetic studies of (AdeH)-$\{Cu^{II}[W^{V}(CN)_8]\}\cdot 2H_2O$ (**1**) ($AdeH^+$, adeninium cations). The new solution provides significantly enlarged interbilayer separation, possible chirality, and the occurrence of nonlinear susceptibility performance in the magnetically ordered state; the last envisaged by full-range angle-resolved monocrystalline magnetic measurements were supported by dedicated calculations.

EXPERIMENTAL SECTION

Precursors were purchased from commercial sources (Sigma-Aldrich, Idalia, Alfa Aesar) or synthesized using literature methods.[53] SC XRD (model **1**) data were collected on BESSY II synchrotron BL14−3 beamline (Helmholtz Zentrum Berlin, Bessy II)[54] and processed with *xdsapp*[55,56] and CrysAlis Pro[57] (absorption correction), SHELXS and SHELX 2018/1[58] (solution and refinement), and WinGx/ROTAX[59] (solution of twinning) softwares. PXRD data (model **1p**) were processed using EXPO2014[60] (indexing and preliminary structure model), FOX[61] (structure determination and optimization), and JANA2006[62] (refinement) software, considering the previous bilayer structural model[39] and CSD entries containing $AdeH^+$ cations.[63] All structural figures were prepared in Mercury.[64] Continuous shape measure analysis of coordination spheres was carried out using SHAPE 2.1.[47] The crystal structures are deposited in the CCDC database, with the deposition numbers 2058785 (model **1**) and

https://doi.org/10.1021/acs.inorgchem.1c00432
Inorg. Chem. 2021, 60, 10186−10198

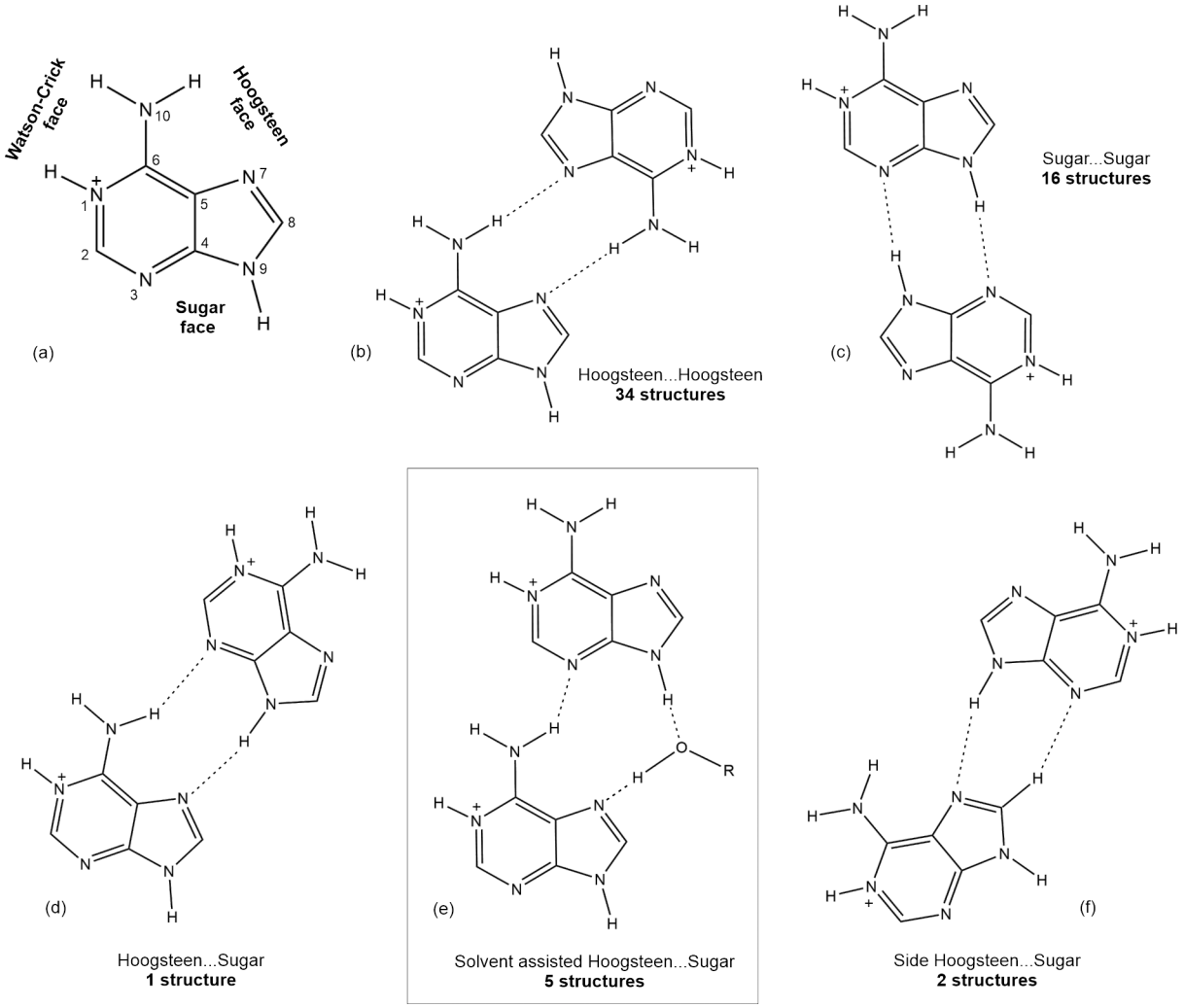

Figure 2. (a) Location of the Hoogsteen face, the sugar face and the Watson−Crick face in $AdeH^+$. (b−f) Dimeric in-plane synthons between $AdeH^+$ cations based on CSD data (2020.1) together with their counts, including the synthon observed in **1** (e). Protonation at the N^1 atom was assumed on the basis of literature data.[65−70] The detailed constrains and the full list of structures (CSD refcodes) are presented in Figure S5 and Table S1.

2058786 (model **1p**). The detailed description of synthesis procedures, crystal data collection, crystal structure determination and refinement, as well as physical methods are available in Figures S1−S3, and S4a and Tables S1−S3.

RESULTS AND DISCUSSION

$AdeH^+$ as a Supramolecular Tecton. $AdeH^+$ cations form parallel planar or close-to-planar side $\{AdeH^+\cdots AdeH^+\}$ synthons (Figures 2 and S5 and Table S1) exploiting interactions between their distinguished regions of the Hoogsteen face ($HN^{10}-C^6-C^5-N^7$), and the sugar face ($N^3-C^4-N^9H$) (for an example description and location of protons, see refs 65−70; Figure 2a). The full record of crystal structures detected includes: 34 cases with the Hoogsteen···Hoogsteen synthon (Figure 2b), 16 cases with the sugar···sugar synthon (Figure 2c), and finally 8 cases with various Hoogsteen···sugar synthons, counting 1 structure with a direct contact (Figure 2d), 5 structures with solvent-assisted contacts, (Figure 2e), and 2 structures exhibiting a contact between the sugar face and the N^7C^8H side fragment of the Hoogsteen face (Figure 2f). The third region, the protonated Watson−Crick face ($HN^{10}-C^6-N^1-H$) for the obvious reason is not involved in the $\{AdeH^+\cdots AdeH^+\}$ synthons; instead, it usually binds nucleophilic entities (mostly anions). The aforementioned planar synthons are frequently accompanied by the parallel or offset parallel $\pi-\pi$ interactions with interplanar distance down to ca. 3.1 Å (Figures 3 and S6, Table S2). Such a diversity of intermolecular $\{AdeH^+\cdots AdeH^+\}$ synthons and their tendency to form stacked arrangement offers the perspective of using the related *infinite cationic blocklike synthons* for molecular crystal engineering.

Structural Studies. The crystal structure of **1** was determined after a thorough analysis of SC XRD data obtained using synchrotron radiation (model **1**). The crystal data and structure refinement parameters are presented in Table S3. **1** crystallizes within the monoclinic *C*2 space group (a = 41.3174(12), b = 7.0727(3), c = 7.3180(2) Å, β = 93.119(3)°, and V = 2135 $Å^3$).

Detailed information on the intralayer distances, bond lengths, angles, and types of coordination polyhedra are presented in the upper section of Table 1 and in Figure S7 and Tables S4 and S5. The topological motif of the 2D cyanido-bridged network $\{Cu^{II}[W^V(CN)_8]^-\}_n$ with four equatorial and one axial cyanido-bridged linkage was reproduced (Figure 4a).

https://doi.org/10.1021/acs.inorgchem.1c00432
Inorg. Chem. 2021, 60, 10186−10198

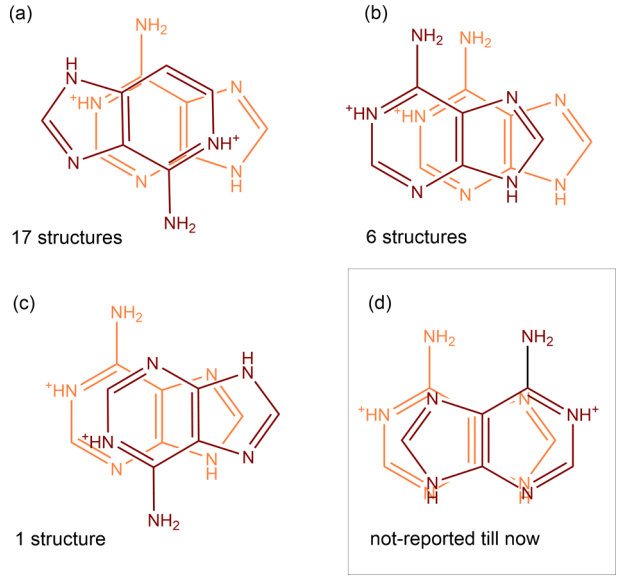

Figure 3. Dimeric parallel or offset parallel synthons between the adeninium cations based on CSD data (2020.1) together with their counts (a–c). The synthon observed in **1** was not observed in database until now (d). The distance between the neighboring AdeH$^+$ planes is not higher than 3.7 Å. The detailed constraints and a full list of the related CSD reference codes are presented in Figure S6 and Table S2.

Table 1. Most Important Intermetallic, Intralayer, and Interlayer Distances in Structural Model 1 and Their Comparison with the Previously Reported Compounds

	1	tetrenH$_5^{5+}$ CuW[39]	dienH$_3^{3+}$ CuW[40]	Cs$^+$ CuW[41]	guaH$^+$ CuW[42]
(a) Average Intralayer Distances (Å)					
Cu$_{eq}$–W[a]	5.24	5.25	5.24	5.25	5.24
Cu$_{ax}$–W	5.44	5.44	5.44	5.44	5.43
Cu–Cu[b]	6.89	6.89	6.88	6.91	6.89
W–W[b]	7.81	7.81	7.81	7.80	7.81
(b) Average Interlayer Distances (Å)					
Cu···Cu[c]	**16.89**	12.40	12.21	11.40	12.19
Cu···W[c]	**15.64**	11.24	11.06	10.16	10.96
W···W[c]	**14.44**	9.97	9.80	9.12	9.84
W$_{planes}$[d]	**13.92**	9.34	9.15	8.20	8.94
Cu$_{planes}$[d]	**16.46**	11.89	11.70	10.67	11.47
(c) Magnetic Properties					
T_c/K	32	34	34	32.8	30
H_c/Oe	60	80	225	300	90

[a]The average distance between the central atom and 4 adjacent atoms [b]The average distance between the central atom and 8 adjacent atoms. [c]The average distance between the central atom of one bilayer and the nearest atoms from the neighboring layer. [d]The distance between two planes determined by positions of corresponding atoms from the first layer and from the neighboring layer.

The Cu$_{eq}$···W distances (5.23–5.26 Å) are significantly shorter compared to the Cu$_{ax}$···W distance (5.44 Å), in a good agreement with the data shown previously.[39−42] The underlying bond lengths Cu–N$_{eq}$ (1.92–2.04 Å), Cu–N$_{ax}$ (2.129 Å), W–C (2.09–2.19 Å), and C–N (1.09–1.20 Å), and the relevant angles W–C–N (172.8–176.3°), Cu–N–C$_{eq}$ (167.4–175.3°) and Cu–N–C$_{ax}$ (177.4°) are in line with the recently investigated structural models. The directions of equatorial cyanido-bridges are oriented diagonally with respect

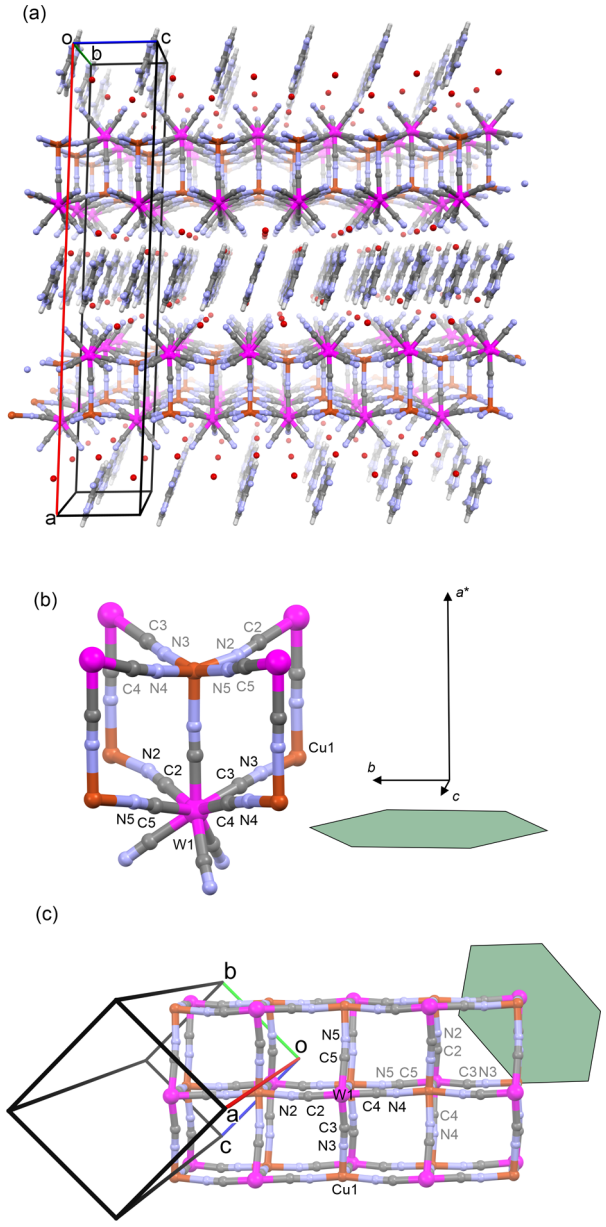

Figure 4. Crystal structure of **1**. (a) 3D architecture showing anionic coordination double layers $\{Cu^{II}[M^{V}(CN)_8]\}^-$ separated by AdeH$^+$ cations (see also Figures 2e and 5). (b, c) Fragments of coordination backbone showing the arrangement of cyanido-bridged linkages along the bilayer, crystallographic directions, and atom numbering according to the SC XRD model **1**. The hexagonal green shape fairly illustrates the crystal habit and its orientation in respect to the crystallographic directions and cyanido-bridged linkages. Colors: W, pink; Cu, brick; C, gray; N, pale blue; O, red.

to the crystallographic directions *b* and *c*, whereas the axial bridges are parallel to the direction *a**. The $\{\cdots N3–Cu–N5C5–W–C3\cdots\}_\infty$ and $\{\cdots N2–Cu–N4C4–W–C2\cdots\}_\infty$ linear chains forming square grid arrangement in the bottom deck of the bilayer are also perpendicular to those in the top deck (Figure 4b,c), and this feature is repeated in each bilayer.

The illustrative data on interlayer separation are shown in the bottom section of Table 1. All examined parameters, the closest Cu···Cu, Cu···W, and W···W separations, together with the closest distances between the planes formed by Cu atoms (or W atoms) belonging to the neighboring layers (W$_{planes}$ and

https://doi.org/10.1021/acs.inorgchem.1c00432
Inorg. Chem. 2021, 60, 10186−10198

Cu_{planes}, respectively), indicate a significant increase of the interlayer separation of ca. 50% compared to the former analogues in this family. This was achieved owing to the specific molecular 2D arrangement of the adeninium $AdeH^+$ cations combining the in-plane contacts and stacking contacts, as illustrated in Figure 5 and Table 2. The in-plane $AdeH^+$···

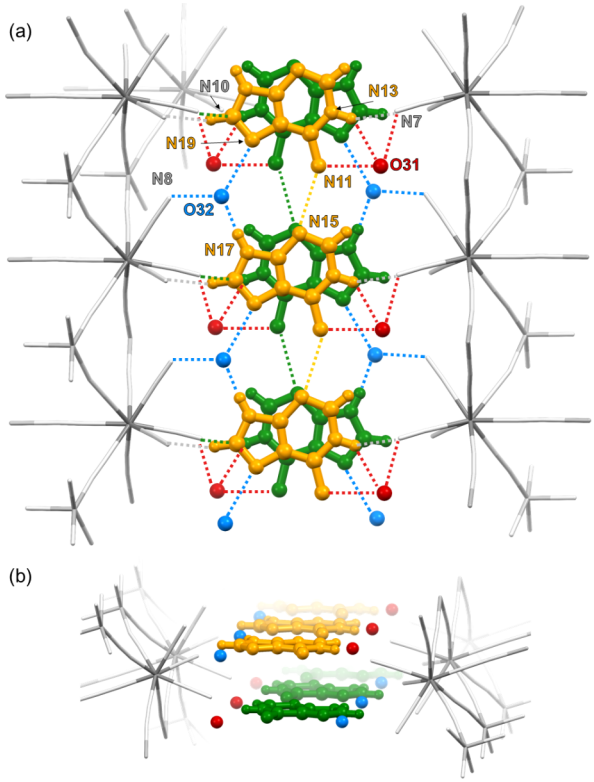

Figure 5. Illustration of hydrogen bonds and short contacts in **1**. Color code: green and orange, $AdeH^+$ cations in two adjacent planes; red, oxygen atom of $H_2O(31)$ molecules located slightly out of the $AdeH^+$ plane; blue, oxygen atom of $H_2O(32)$ molecules located in the $AdeH^+$ plane; gray scale, coordination skeleton of the $Cu^{II}W^{V}$ bilayer. For details see Table 2. Compare with Figure 2e.

Table 2. H-Bonds Donor···Acceptor Distances in 1[a]

D	A	d_{DA}	$d_{DA} - \sum VdW$	angle D−H···A[deg]
N7	N13	2.87	−0.24	150
N10	N13	3.07	−0.03	105
N7	O31	2.62	−0.45	
N8	O32	2.53	−0.54	
N15	N11	3.06	−0.04	
O31	N11	2.70	−0.37	
N19	O32	2.80	−0.274	
O32	N17	2.68	−0.394	175

[a]The role of donor (D) and acceptor (A) were determined intuitively, where required.

$AdeH^+$ synthons are arranged into infinite $\{AdeH^+\}_n$ ribbons *via* direct double-strand contacts between the Hoogsteen face ($HN^{10}-C^6-C^5-N^7$) and the Sugar face ($N^3-C^4-N^9H$), here realized by the N15···H−N11 contact (d_{NN} = 3.06 Å) (N^3···$H-N^{10}$) accompanied by the N19···H−O32···H−N17 contact (d_{NO} = 2.80 and 2.68 Å) (N^7···H−O···H−N^9) (compare Figure 2a,e). The O32 atom of the water molecule forms also a contact with the N8C8 terminal cyanide, most probably acting as the hydrogen donor. The supramolecular architecture is completed with a contact between the protonated Watson−Crick face ($HN^{10}-C^6-N^1-H$) and O31 water molecule (N11···O31 = 2.70 Å), which is additionally bound to the N7C7 cyanide at the other side of $\{AdeH^+\}_n$ ribbon (O31···N7 = 2.62 Å). The neighboring ribbons are parallel to each other and form infinite stacks within 2D interlayer space, with the interplane distance of ca. 3.4 Å. Within this arrangement, the sugar faces are projected onto each other at the one side of the stack, and the Hoogsteen faces are projected onto each other at the second side. However, the protonated Watson−Crick faces are exposed remotely outside the center of $AdeH^+$. It is important to note that the in-plane solvent-assisted Hoogsteen···sugar synthons observed in **1** were realized previously in crystal structures of 5 literature compounds (CSD crystal structure refcodes EGOWIG, LOLDEW, LOLDIA, UWAMEM, and UWAMEM1; Figure 2e) exclusively involving monoprotonated $AdeH^+$ synthons. This significantly supports a reliability of our observation. The C−C and C−N distances in $AdeH^+$ cations are close to those found in the reference literature data (Figures S8, and S9, Table S6).

Analysis of the PXRD data (see model **1p**, Figures S10 and S11, Tables S3, S7, and S8) showed the presence of $\{Cu^{II}[M^{V}(CN)_8]\}^-$ bilayers, $AdeH^+$ cations, and crystallization H_2O molecules in **1**. It also confirmed a crucial role of the latter components in shaping of the interbilayer separation in **1** (for more detail, see the Supporting Information).

Chirality that could occur in the space group *C*2 is canceled by a 4-component twinning involving inversion operation necessary to model the crystal structure in SC XRD data analysis; however, the specific bilayer arrangement observed for the single primary grain will have substantial impact on magnetic properties. The twinning is dominated by the component obtained through the inversion operation of the original grain structure (47.5%) and completed by other minor components issued by the C_2 rotation with respect to the [100] direction (2.27%, see the description of TWIN command in the CCDC file), and by a combination of this rotation with the inversion operation (3.26%). Considering the fact that magnetization is a pseudovector (it does not change under the inversion operation), such twinning composition should not influence the magnetic properties.

Magnetic Properties. Magnetic measurements for a batch of single crystals were carried out along three orthogonal directions, *H*||*a**, *H*||*b*, and *H*||*c*, indicated by indexing procedure and in accordance with solution model **1** (Figure S12). Figure 6 shows the temperature dependences of χT products with an applied field of 500 Oe. In the case of *H*||*b* and *H*||*c* orientations, a sharp increase of χT values start below 40 K, whereas for the direction perpendicular to the layer (*H*||*a**), a noticeable growth can be observed below 35 K. For all orientations, the maximum values were recorded at T_{peak} = 28.0 K, reaching 1130 $cm^3\ mol^{-1}$ K for *H*||*b*, 1202 $cm^3\ mol^{-1}$ K for *H*||*c*, and 84 $cm^3\ mol^{-1}$ K for *H*||*a**. It is clear that the magnetization prefers to align within the double-layer (within the *bc* plane), while the perpendicular direction, with the response more than 1 order of magnitude smaller, is the hard axis. However, much smaller but still noticeable differences can be observed between the two in-plane orientations. These dissimilarities are more evident in low field (50 Oe) ZFC/FC measurements (Figure 7 and S13), which show stronger difference between field-cooled and zero-field-cooled curves for *H*||*c* orientation than for those *H*||*b*. This suggests a more

https://doi.org/10.1021/acs.inorgchem.1c00432
Inorg. Chem. 2021, 60, 10186−10198

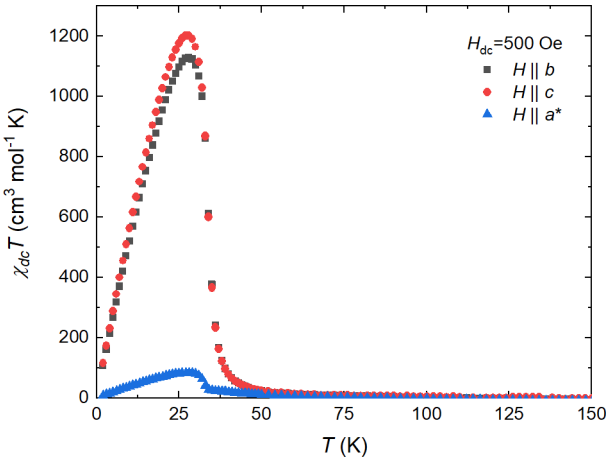

Figure 6. Temperature dependence of χT for **1** as measured at 500 Oe for *H*||*b* (black squares), *H*||*c* (red circles), and *H*||*a** (blue triangles).

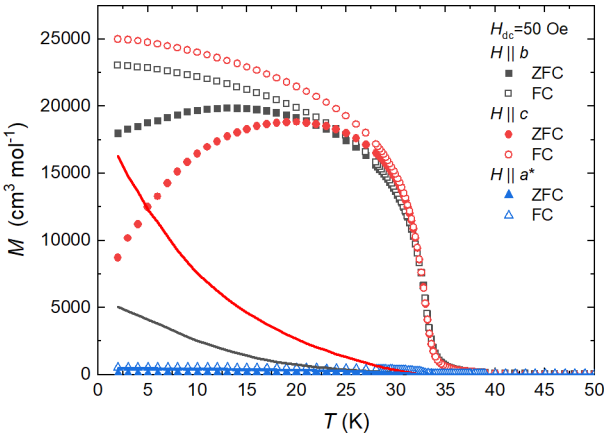

Figure 7. Zero-field-cooled (full symbols) and field-cooled (empty symbols) magnetization for H_{dc} = 50 Oe as a function of temperature for *H*||*b* (black squares), *H*||*c* (red circles), and *H*||*a** (blue triangles). The solid lines show the difference between the FC and ZFC data.

complex anisotropy than the simple easy plane type. A notable divergence between ZFC and FC curves starts for all orientations at a similar temperature of about 32.6 K (Figure S13), while the T_c temperature, determined from the first derivative of ZFC susceptibility (Figure S14), is slightly higher: T_C = 32.8(2) K for *H*||*a**, T_c = 33.2(2) K for *H*||*b*, and T_c = 33.0(2) K for *H*||*c*.

Isothermal magnetization measurements at 2.0 K (Figure 8) indicate that **1** saturates for *H*||*b* and *H*||*c* for fields above 10 kOe at 2.0 μ_B/f.u., which agrees with the expected value for the parallel alignment of the Cu^{II} (S_{Cu} = 1/2, g_{Cu} = 2.0) and W^V (S_W = 1/2, g_W = 2.0) magnetic moments per $\{Cu^{II}[W^V(CN)_8]\}^-$ unit. In contrast, the applied field in the perpendicular direction, even at 70 kOe, is too weak to reach saturation, which points to a significant magnetic anisotropy. Within a double-layer, **1** displays a rather soft magnetic behavior with the small coercive field of 60 Oe, whereas coercivity for *H*||*a** is 1 order of magnitude higher reaching 750 Oe.

Both the isothermal magnetization and the temperature dependence of magnetic susceptibility points to a ferromagnetic behavior with significant intramolecular interactions within the *bc* plane. Since the interbilayer separation is

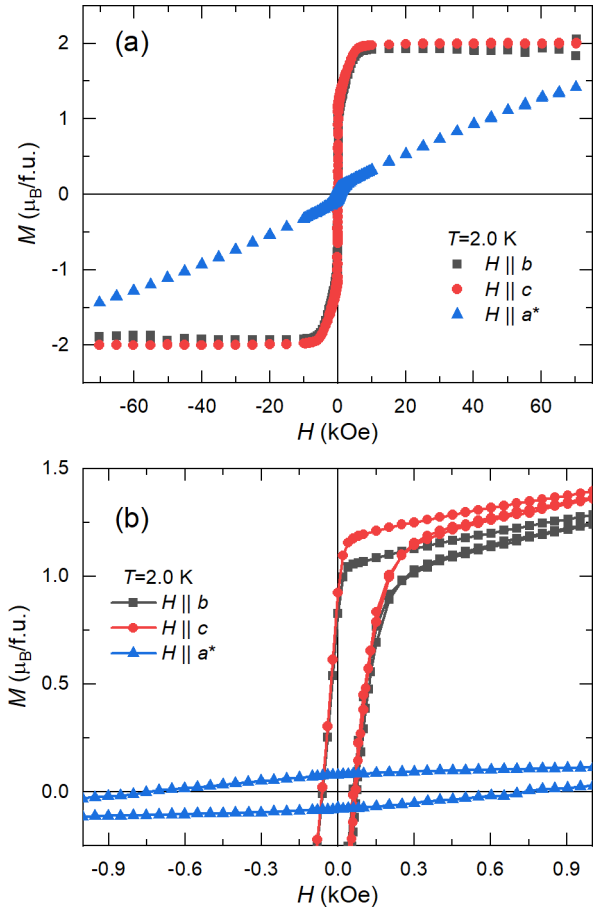

Figure 8. Isothermal magnetization at 2.0 K for *H*||*b* (black squares), *H*||*c* (red circles), and *H*||*a** (blue triangles) orientations.

substantial (about 14.5 Å) and there is no direct linkage between the planes, the most obvious candidate for interbilayer interaction is the dipole−dipole coupling.

Angle-Resolved Susceptibilities. The magnetic susceptibility was measured within three independent planes, i.e., the plane perpendicular to the *a** crystallographic axis, the plane perpendicular to the *b* crystallographic axis, and the plane perpendicular to the *c* crystallographic axis, with the angle step of 5° in the applied field of 1 kOe at 2 K, using a Quantum Design Horizontal Sample Rotator and Quantum Design MPMS XL magnetometer. The raw data were corrected for diamagnetic contribution using the orientation averaged value of $\chi_0 \approx -0.015$ cm^3 mol^{-1} per formula unit (see Figures S15 and S16). The measurement results shown in Figure 9 confirm that the *a** crystallographic axis corresponds to the hard magnetization direction, while the *bc* crystallographic plane constitutes the easy magnetization plane.

There is, however, one additional striking feature of angle-resolved measurements: A rotation within the easy plane (*bc*) indicates the presence of a 4-fold axis, which contrasts with 2-fold symmetry indicated by rotations within the planes parallel to the hard axis (*a***b* and *ca**). This feature cannot be explained within the linear paradigm, where only the second-rank susceptibility tensor $\chi_{\alpha\beta}$ is employed. To check if a 4-fold axis is a common feature of the Cu^{II}−W^V double-decker topological Prussian blue analogues family, angle-resolved measurement of $(tetrenH_5)_{0.8}\{Cu^{II}[W^V(CN)_8]_4\}\cdot 7.2H_2O\}_n$[48,71] (**2**) (Figure 10) was carried out within the *ac*

https://doi.org/10.1021/acs.inorgchem.1c00432
Inorg. Chem. 2021, 60, 10186−10198

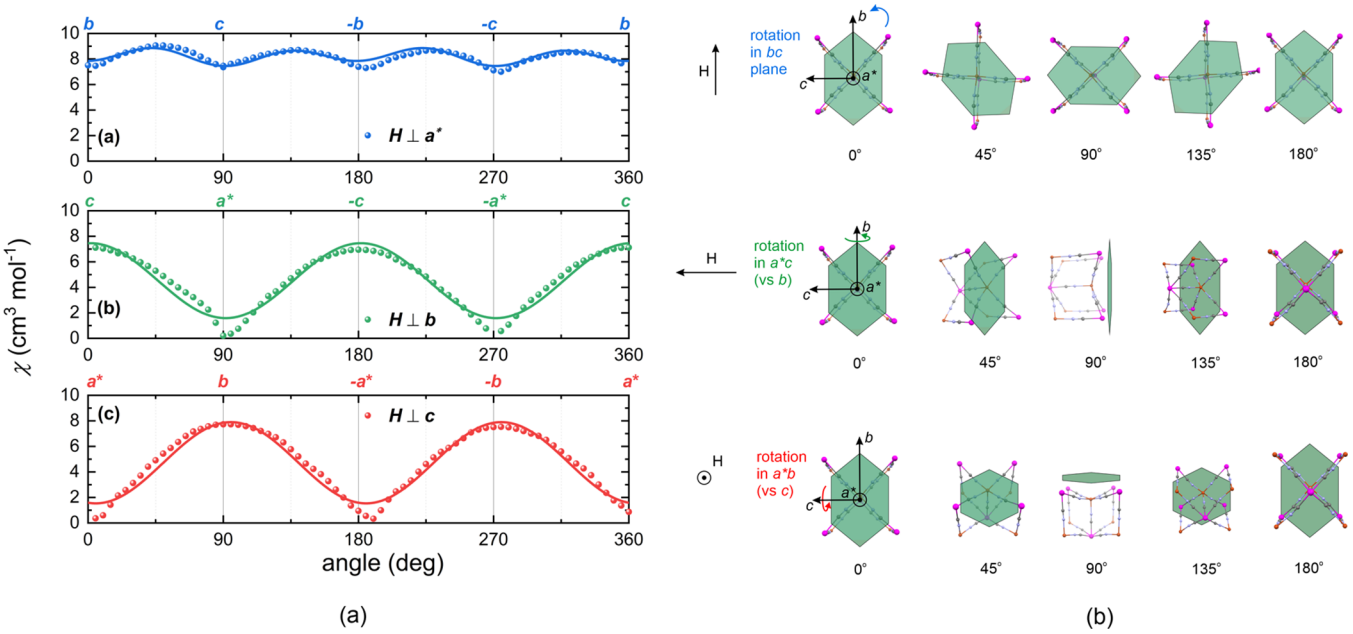

Figure 9. Angle-resolved monocrystalline magnetic measurements: (a) magnetic susceptibility in three independent crystallographic planes at 2 K (solid lines show the best fit of the nonlinear model); (b) the respective orientations of the statistic rotated crystals in the SQUID cavity in respect of the direction of the external magnetic field. Curved arrows show the rotation of the crystal. The hexagonal crystal's shape in the figure fairly illustrates the real crystal's shape (compare Figure S12).

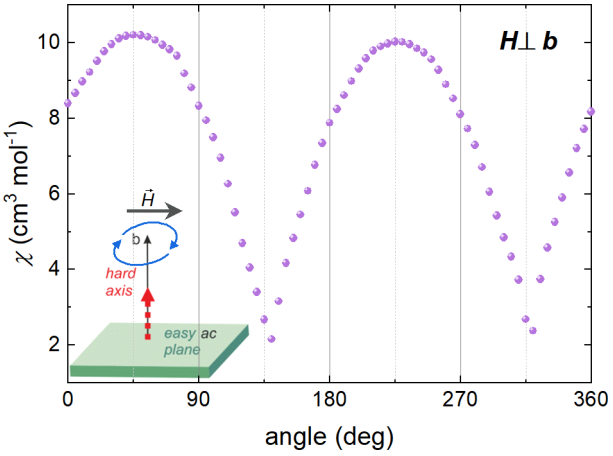

Figure 10. Angle-dependent dc susceptibility of $(tetrenH_5)_{0.8}\{Cu^{II}[W^{V}(CN)_8]_4\}\cdot 7.2H_2O\}_n$ (**2**)[48] at 2.0 K and in 1 kOe applied field.

easy plane, with respect to the direction b, and perpendicular to crystal plane. Although the crystal structures of **1** and **2** are very similar to each other, the latter compound shows only a 2-fold axis. It could be that in the case of **2** the applied field is too weak to reveal the nonlinear behavior; however, this issue will be analyzed in more detail in further studies. In what follows, we will show within a simplified model that the 4-fold symmetry in **1** can be roughly reproduced assuming a higher-order contribution to the susceptibility which is nonlinear in the applied field.

Let us expand the magnetization pseudovector in a series of the applied magnetic field:

$$M_\alpha = M_\alpha(\vec{H}=\vec{0}) + \chi_{\alpha\beta}(\vec{H}=\vec{0})H_\beta + \frac{1}{2!}\tau_{\alpha\beta\mu}(\vec{H}=\vec{0})H_\beta H_\mu + \frac{1}{3!}\kappa_{\alpha\beta\mu\nu}(\vec{H}=\vec{0})H_\beta H_\mu H_\nu + O(H^4) \quad (1)$$

where the Einstein summation rule over repeated indices has been assumed. The relation $M_\alpha(-\vec{H}) = -M_\alpha(\vec{H})$ eliminates all even field terms in the expansion in eq 1, so that $M_\alpha(\vec{H}=\vec{0}) = 0$ and $\tau_{\alpha\beta\mu}(\vec{H}=\vec{0}) = 0$ for all $\alpha, \beta, \mu \in \{a^*, b, c\}$. Thus, the measured susceptibility $\chi(\vec{H})$ corresponding to the applied field vector $\vec{H}$ reads

$$\chi(\vec{H}) = \frac{M_\alpha H_\alpha}{|\vec{H}|^2} = \chi_{\alpha\beta}\frac{H_\alpha}{|\vec{H}|}\frac{H_\beta}{|\vec{H}|} + \frac{1}{6}|\vec{H}|^2\kappa_{\alpha\beta\mu\nu}\frac{H_\alpha}{|\vec{H}|}\frac{H_\beta}{|\vec{H}|}\frac{H_\mu}{|\vec{H}|}\frac{H_\nu}{|\vec{H}|} + O(|\vec{H}|^4) \quad (2)$$

where

$$\vec{H}(\theta) = \begin{cases} H_0[0, \cos\theta, \sin\theta] \text{ for rotation around the } a^* \text{ axis} \\ H_0[\sin\theta, 0, \cos\theta] \text{ for rotation around the } b \text{ axis} \\ H_0[\cos\theta, \sin\theta, 0] \text{ for rotation around the } c \text{ axis} \end{cases} \quad (3)$$

with H_0 = 1 kOe and the rotation angle $\theta \in [0, 360°)$. We assume that the susceptibility linear tensor $\chi_{\alpha\beta}$ is symmetric, i.e., $\chi_{\alpha\beta} = \chi_{\beta\alpha}$, while the only nonvanishing components of the nonlinear tensor $\kappa_{\alpha\beta\mu\nu}$ are those with indices $bbcc$ and all different permutations thereof. Moreover, we assume that they are all equal as being of the same symmetry, i.e., $\kappa_{bbcc} = \kappa_{bccb} = \kappa_{ccbb} = \kappa_{cbbc} = \kappa_{bcbc} = \kappa_{cbcb} \neq 0$. Then, a straightforward calculation using eqs 2 and 3 yields

$$\chi_{a^*}(\theta) = \frac{1}{2}(\chi_{bb} + \chi_{cc}) + \frac{1}{2}(\chi_{bb} - \chi_{cc})\cos 2\theta + \chi_{bc}\sin 2\theta + \kappa\sin^2\theta\cos^2\theta \quad (4)$$

https://doi.org/10.1021/acs.inorgchem.1c00432
Inorg. Chem. 2021, 60, 10186−10198

Table 3. Parameter Values Corresponding to the Best Fit of the Nonlinear Model to the Angle-Resolved Susceptibility Data

parameter	$\chi_{a^*a^*}$ [cm^3 mol^{-1}]	χ_{bb} [cm^3 mol^{-1}]	χ_{cc} [cm^3 mol^{-1}]	χ_{a^*b} [cm^3 mol^{-1}]	χ_{bc} [cm^3 mol^{-1}]	χ_{ca^*}[cm^3 mol^{-1}]	κ [cm^3 mol^{-1}]
parameter value	1.59	7.85	7.45	−0.565	0.102	0.166	4.38
standard relative error [%]	4.0	0.89	0.92	13	73	44	10

$$\chi_b(\theta) = \frac{1}{2}(\chi_{cc} + \chi_{a^*a^*}) + \frac{1}{2}(\chi_{cc} - \chi_{a^*a^*})\cos 2\theta + \chi_{a^*c}\sin 2\theta \quad (5)$$

$$\chi_c(\theta) = \frac{1}{2}(\chi_{a^*a^*} + \chi_{bb}) + \frac{1}{2}(\chi_{a^*a^*} - \chi_{bb})\cos 2\theta + \chi_{a^*b}\sin 2\theta \quad (6)$$

where $\kappa = H_0^2\kappa_{bbcc}$. Equations 4−6 have been simultaneously fitted to the experimental angle-resolved susceptibility data using the following test function (agreement quotient)

$$Q_\chi = \sum_{A\in\Omega} \frac{\sum_i [\chi_{A,i} - \chi_A(\theta_i)]^2}{\sum_j [\chi_{A,j}]^2} \quad (7)$$

where $\Omega = \{a^*, b, c\}$ is the set of the rotation axes. The best fit yielded $Q_\chi = 2.02 \times 10^{-2}$ and the set of parameter values listed in Table 3. The solid lines in Figure 8 show the best-fit curves.

One can see that the agreement with the experimental data is satisfactory but by no means perfect. The main feature of the data, i.e., the fact that rotations within the planes parallel to the hard axis (a^*b and ca^*, red and green, respectively, in Figure 9) reveal the presence of a 2-fold axis, while a rotation within the easy plane (bc, blue in Figure 9) indicates the presence of a 4-fold axis and is duly reproduced. However, the present model fails to reproduce the low-value kinks observed for rotations around the b axis (green in Figure 9) and c axis (red in Figure 9). This may be understandable due to the fact that the model in its present shape is crucially simplified, neglecting 75 out of 81 components of the nonlinear susceptibility tensor $\kappa_{\alpha\beta\mu\nu}$. However, the exceptionally large relative error for χ_{bc} together with its relatively small absolute value make it practically redundant, showing that the model may be even further simplified. It is worth noting that the component χ_{bc} would automatically vanish if one assumed that the system is composed of two sublattices transformed one into another by the 90° rotation around the hard axis (a^* crystallographic axis). Then, the components $\kappa_{bbcc} = \kappa_{bccb} = \kappa_{ccbb} = \kappa_{cbbc} = \kappa_{bcbc} = \kappa_{cbcb} \neq 0$ of the nonlinear susceptibility tensor of the fourth rank give the first nonzero contribution in its place. The $\{\cdots$N3−Cu−N5C5−W-C3$\cdots\}_\infty$ and $\{\cdots$N2−Cu−N4C4−W-C2$\cdots\}_\infty$ linear chains forming square grid arrangement in the bottom deck of the bilayer are also perpendicular to those in the top deck and this feature is repeated in each bilayer.

In the above model, the nonzero components of the nonlinear susceptibility tensor $\kappa_{\alpha\beta\mu\nu}$ are crucial to reproduce the 4-fold symmetry axis for a rotation around the hard magnetization direction (a^* crystallographic axis). At the same time, they give rise to an interesting feature of the total susceptibility tensor $\chi_{a^*\alpha\beta}$ associated with that rotation:

$$\chi_{a^*\alpha\beta}(\theta) = \chi_{\alpha\beta} + \frac{1}{6}H_0^2\kappa_{\alpha\beta\mu\nu}\frac{H_{a^*\mu}(\theta)}{|\vec{H}_{a^*}(\theta)|}\frac{H_{a^*\nu}(\theta)}{|\vec{H}_{a^*}(\theta)|} \quad (8)$$

where $\vec{H}_{a^*}(\theta)$ is given by the first row in eq 3. It is apparent from eq 8 that due to the nonlinear susceptibility term the total susceptibility tensor $\chi_{a^*\alpha\beta}$ becomes dependent on the orientation of the applied magnetic field expressed in terms of the rotation angle θ. Hence its eigenvalues and eigenvectors will also depend on the applied field orientation. Figures 11

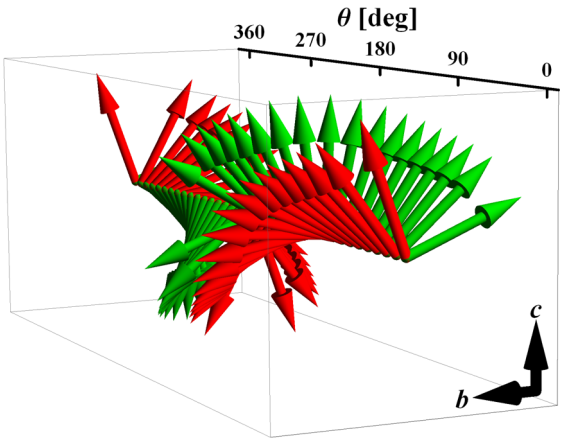

Figure 11. Rotation of eigenvectors of $\chi_{a^*\alpha\beta}$ corresponding to the largest (red) and the second largest (green) eigenvalue as a function the orientation angle of the applied magnetic field $\vec{H}_{a^*}(\theta)$.

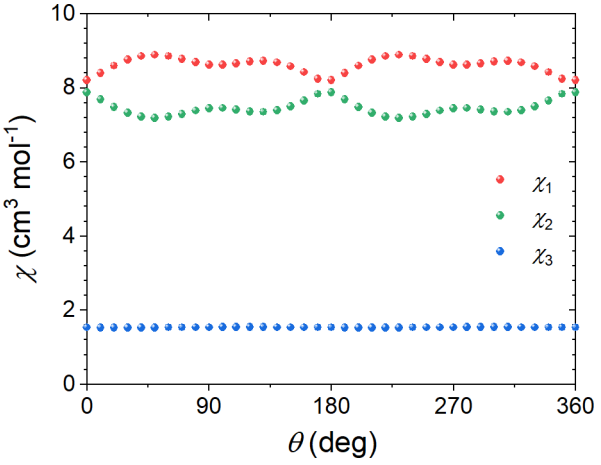

Figure 12. Dependence of the eigenvalues of $\chi_{a^*\alpha\beta}$ on the orientation angle of the applied magnetic field $\vec{H}_{a^*}(\theta)$.

and 12 show this dependence. It can be seen that the eigenvectors corresponding to the largest and the second largest eigenvalues lie in the bc easy plane and rotate in an anticlockwise sense around the a^* axis with a rotation of the applied field $\vec{H}_{a^*}(\theta)$. In this way, the direction of the external magnetic field coincides with the direction of the easy axis (red arrows in Figure 11) four times for angles θ roughly equal to 45, 135, 225, and 315°, which correspond to the local maxima of the largest eigenvalue (red symbols in Figure 12).

The quality of fit of the angle-resolved susceptibility data may be improved by adding to the present model other components of the four-rank tensor $\kappa_{\alpha\beta\mu\nu}$ as well as by

https://doi.org/10.1021/acs.inorgchem.1c00432
Inorg. Chem. 2021, 60, 10186−10198

extending the magnetization expansion in eq 1 to even higher orders. This is corroborated by the trigonometric polynomial approximation (see the Supporting Information).

Scaling Analysis. The ordering process in **1** was analyzed with the static critical scaling of the magnetic susceptibility. To unambiguously obtain the values of γ and T_C, we have used the approach described in a series of papers.[72−75] Figure 13 shows

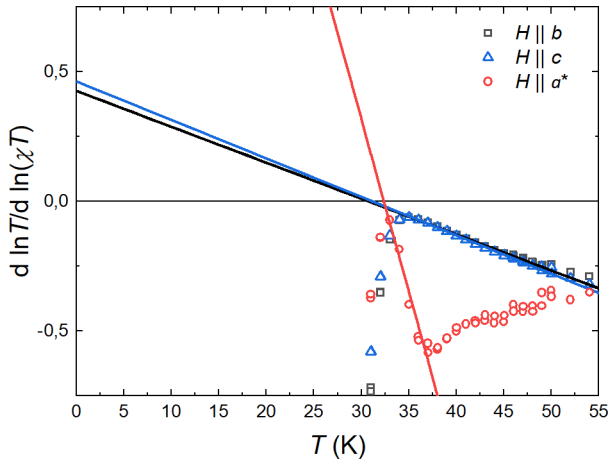

Figure 13. Critical scaling of the magnetic susceptibility. Solid lines show the linear fits to the rescaled χT values.

the temperature dependence of the $d(\ln(T))/d(\ln(\chi T))$. Linear fits above the phase transition were used to determine γ (the inverse value of the intersection point with the ordinate axis) and T_C (the intersection with the abscissa axis). The fitting of critical exponents were done between $\approx T_c$ and $\approx 1.2T_c$ (about 33−40 K) in case of in-plane orientations and between $\approx T_c$ and $\approx 1.1T_c$ for the hard axis. Both in-plane fits points to high value of the critical exponents $\gamma_b = 2.34(6)$ (for $H \| b$) and $\gamma_c = 2.16(5)$ (for $H \| c$) with similar temperatures of the phase transition $T_{C\text{-}b} = 30.8(2)$ K (for $H \| b$) and $T_{C\text{-}c} = 31.1(2)$ K (for $H \| c$). The data for the out-of-plane orientation show a similar value of $T_{C\text{-}a^*} = 32.4(2)$ K; however, the critical exponent for the $H \| a^*$ $\gamma_{a^*} = 0.23(2)$ is 1 order of magnitude lower than for the in-plane orientation. The low value of γ_{a^*} points to a very weak temperature dependence of the susceptibility for the hard axis below T_C, which underlines the dominant role of the ordering within the bc plane and is symptomatic for 2D magnetism.[71]

The scaling analysis in both in-plane directions ($H \| b$ and $H \| c$) has revealed high values of γ pointing to 2D ordering process like 2D XY ($\gamma = 1.82$)[76] or 2D XXZ ($\gamma = 2.17(5)$)[77] instead of 3D ones, which are characterized with much lower value of γ (3D Heisenberg $\gamma = 1.385$, 3D Ising $\gamma \approx 1.24$ or 3D XY $\gamma = 1.32$).[78] The 2D character of the magnetic phase transition can be related to the Berezinskii−Kosterlitz−Thouless topological phase transition in which the bonding of vortex−antivortex pairs occurs below T_{BKT} critical temperature.[79−81] In this case, the magnetic susceptibility follows $\chi T = a_\chi \, e^{b_\chi (T - T_{BKT})^{-\nu}}$ with the critical exponent $\nu = 0.5$. The above equation was used to analyze the susceptibility in both in-plane directions (Figure 14 and S19; the fitting ranges were the same as in the case of γ scaling) revealing: $\nu_b = 0.48(5)$, $T_{BKT\text{-}b} = 29.6(3)$ K, $a_{\chi\text{-}b} = 1.1(4)$ emu mol^{-1} K, $b_{\chi\text{-}b} = 13.1(7)$ K$^\nu$ for $H \| b$ and $\nu_c = 0.49(3)$, $T_{BKT\text{-}c} = 29.7(1)$ K, $a_{\chi\text{-}c} = 1.4(2)$ emu mol^{-1} K, $b_{\chi\text{-}c} = 12.6(3)$ K$^\nu$ for $H \| c$. Both obtained values of ν are

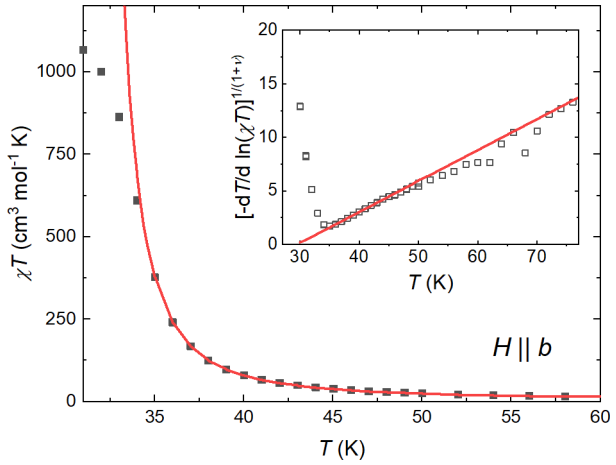

Figure 14. Berezinskii−Kosterlitz−Thouless critical scaling analysis of χT vs T for $H \| b$. Inset shows the indication of the BKT transition for $H \| b$. The red solid line shows the best fit to $\chi T = a_\chi \, e^{b_\chi (T - T_{BKT})^{-\nu}}$.

consistent, within the uncertainty, with the Kosterlitz and Thouless results.

Ferromagnetic 2D ordering within the double-layer and the BKT-type phase transition were also recognized in our previous study of the $\{(tetrenH_5)_{0.8}Cu^{II}_4[W^V(CN)_8]_4 \cdot H_2O\}_n$ (**2**) compound which is built of similar and topologically identical Cu^{II}−W^V bilayers.[71] **2** reveals an LRMO below $T_C \approx 33$ K and the BKT phase transition with $T_{BKT} = 30.3$ K and $\nu = 0.56(11)$. The similarity between both compounds is striking: the intrabilayer separation in **1** is ca. 14.0 Å, while in **2** it is only ca. 9.0 Å. Both cases indicate that the significant anisotropy and interactions within the bilayer play the crucial roles and are responsible for the 2D ordering. However, the dipolar interactions have a minor influence on LRMO because even the sizable difference in the separation between the bilayers does not change the basic ordering parameters of both compounds.

CONCLUSIONS

The adeninium $AdeH^+$ monocations were successfully used in tuning of interlayer separation between the magnetic coordination $\{Cu^{II}[W^V(CN)_8]^-\}_\infty$ bilayers in **1**. The cationic layers are composed of 1D infinite hydrogen-bonded ribbons engaging the Hoogsteen face and the sugar face of $AdeH^+$ together with the crystallization of H_2O molecules; one of the topological hydrogen bond synthons existing in the structural database was reproduced in this way. These ribbons are further connected into 2D architecture by orthogonal π−π stacking, to be finally glued to the bimetallic coordination backbone via hydrogen bonds with the terminal CN^- bridges. The implementation of such a blocklike arrangement led to the significant increase of separation between $\{Cu^{II}[W^V(CN)_8]^-\}_\infty$ bilayers, from ca. 9 to ca. 14 Å, compared to the congeners reported previously. Such combinations of polycationic blocks with polynuclear coordination complexes are relatively rare: Some examples are from the chemistry of polyoxometalates,[82,83] whereas for the first time it is observed in magnetochemistry of polycyanidometalate-based networks.

The complete angle-resolved magnetic measurements confirmed 2D character of magnetic ordering due to a strong magnetic exchange coupling between Cu(II) and W(V) spins within layers, in line with general features observed in the

https://doi.org/10.1021/acs.inorgchem.1c00432
Inorg. Chem. 2021, 60, 10186−10198

family of $\{Cu^{II}[W^{V}(CN)_8]^-\}_\infty$ based compounds. However, several new features were disclosed by this new compound. First, non-negligible magnetic anisotropy was detected within the easy plane, which was not shown experimentally until now. Second, we acquired the nonlinear magnetic susceptibility in a relatively small magnetic field, which was manifested by rare 4-fold symmetry of magnetization detected during the rotation within the easy plane. The observation was rationalized by the calculations using the dedicated model.

The nonlinear magnetic response in a molecular magnet was also investigated by Mito et al. In their research, the $[Cr(CN)_6][Mn(R)\text{-}pnH(H_2O)](H_2O)$ compound was measured with means of alternating current susceptibility and higher harmonics. Authors underlined the role of magnetic softness and chirality for the nonlinear response.[84] In our case, **1** does not reveal chirality; however, the soft magnetic degrees of freedom in the *bc* plane may play the key role in the observed magnetic nonlinear behavior.

Finally, the magnetic $\{Cu^{II}[W^{V}(CN)_8]^-\}_\infty$ backbone was incorporated in the crystal of the *C*2 space group, although the total chirality was canceled due to twinning dominated by the component reproduced by inversion symmetry. Nevertheless, further advances toward the general organization of coordination layers in the solid state can be achieved using organic components with diverse distribution of noncovalent interaction generators. The possible coexistence of BKT topological phase transition (within the regime of controlled *XY* magnetism) with chirality (if successfully acquired within the whole crystal) and nonlinear magnetic susceptibility offers the perspectives for systematic research on the magneto-chiral effects on the "colored" coordination backbones of the related type.[85,86]

■ ASSOCIATED CONTENT

Supporting Information

The Supporting Information is available free of charge at https://pubs.acs.org/doi/10.1021/acs.inorgchem.1c00432.

> Synthesis and basic characterization (materials and syntheses, physical techniques, $AdeH^+$ as a supramolecular tecton, SC XRD studies, PXRD studies); magnetic studies (description of all measurement; estimation of the diamagnetic corrections; trigonometric polynomial expansion for the angle-resolved data; scaling analysis); references (PDF)

Accession Codes

CCDC 2058785 and 2058786 contain the supplementary crystallographic data for this paper. These data can be obtained free of charge via www.ccdc.cam.ac.uk/data_request/cif, or by emailing data_request@ccdc.cam.ac.uk, or by contacting The Cambridge Crystallographic Data Centre, 12 Union Road, Cambridge CB2 1EZ, UK; fax: +44 1223 336033.

■ AUTHOR INFORMATION

Corresponding Authors

Piotr Konieczny − *Institute of Nuclear Physics PAN, 31-342 Kraków, Poland;* orcid.org/0000-0002-0024-9557; Email: piotr.konieczny@ifj.edu.pl

Robert Podgajny − *Faculty of Chemistry, Jagiellonian University, 30-387 Kraków, Poland;* orcid.org/0000-0001-7457-6799; Email: robert.podgajny@uj.edu.pl

Authors

Emilia Kuzniak-Glanowska − *Faculty of Chemistry, Jagiellonian University, 30-387 Kraków, Poland*

Robert Pełka − *Institute of Nuclear Physics PAN, 31-342 Kraków, Poland;* orcid.org/0000-0002-9796-250X

Tadeusz M. Muzioł − *Faculty of Chemistry, Nicolaus Copernicus University in Torun, 87-100 Torun, Poland;* orcid.org/0000-0002-5220-4430

Marcin Kozieł − *Faculty of Chemistry, Jagiellonian University, 30-387 Kraków, Poland;* orcid.org/0000-0002-9606-7642

Complete contact information is available at: https://pubs.acs.org/10.1021/acs.inorgchem.1c00432

Notes

The authors declare no competing financial interest.

■ ACKNOWLEDGMENTS

The present research was financed by National Science Centre, Poland, grant OPUS 18 (2019/35/B/ST5/01481) (R.P.) and grant SONATA No. (2018/31/D/ST8/02118) (P.K.). Diffraction data were collected on BL14.2 and BL14.3 at the BESSY II electron storage ring operated by the Helmholtz-Zentrum Berlin.[54] We would particularly acknowledge the help and support of Dr. Piotr Wilk during the experiment. E.K.-G. acknowledges the fellowship within the project no. POWR.03.02.00-00-I013/16.

■ REFERENCES

(1) Rocha, A. R.; García-Suárez, V. M.; Bailey, S. W.; Lambert, C. J.; Ferrer, J.; Sanvito, S. Towards molecular spintronics. *Nat. Mater.* **2005**, *4*, 335−339.

(2) Cornia, A.; Seneor, P. The molecular way. *Nat. Mater.* **2017**, *16*, 505−506.

(3) Chakraborty, G.; Park, I.-H.; Medishetty, R.; Vittal, J. J. Two-Dimensional Metal-Organic Framework Materials: Synthesis, Structures, Properties and Applications. *Chem. Rev.* **2021**, *121*, 3751−3891.

(4) Coronado, E. Molecular magnetism: from chemical design to spin control in molecules, materials and devices. *Nat. Rev. Mater.* **2020**, *5*, 87−104.

(5) Ohba, M.; Yoneda, K.; Agustí, G.; Muñoz, M. C.; Gaspar, A. B.; Real, J. A.; Yamasaki, M.; Ando, H.; Nakao, Y.; Sakaki, S.; Kitagawa, S. Bidirectional Chemo-Switching of Spin State in a Microporous Framework. *Angew. Chem., Int. Ed.* **2009**, *48*, 4767−4771.

(6) Agustí, G.; Ohtani, R.; Yoneda, K.; Gaspar, A. B.; Ohba, M.; Sánchez-Royo, J. F.; Muñoz, M. C.; Kitagawa, S.; Real, J. A. Oxidative Addition of Halogens on Open Metal Sites in a Microporous Spin-Crossover Coordination Polymer. *Angew. Chem., Int. Ed.* **2009**, *48*, 8944−8947.

(7) Muñoz-Lara, F. J.; Gaspar, A. B.; Muñoz, M. C.; Ksenofontov, V.; Real, J. A. Novel Iron(II) Microporous Spin-Crossover Coordination Polymers with Enhanced Pore Size. *Inorg. Chem.* **2013**, *52*, 3−5.

(8) Liu, W.; Wang, L.; Su, Y. J.; Chen, Y. C.; Tucek, J.; Zboril, R.; Ni, Z. P.; Tong, M. L. Hysteretic Spin Crossover in Two-Dimensional (2D) Hofmann-Type Coordination Polymers. *Inorg. Chem.* **2015**, *54*, 8711−8716.

(9) Piñeiro-López, L.; Valverde-Muñoz, F. J.; Seredyuk, M.; Muñoz, M. C.; Haukka, M.; Real, J. A. Guest Induced Strong Cooperative One- and Two-Step Spin Transitions in Highly Porous Iron(II) Hofmann-Type Metal−Organic Frameworks. *Inorg. Chem.* **2017**, *56*, 7038−7047.

(10) Murphy, M. J.; Zenere, K. A.; Ragon, F.; Southon, P. D.; Kepert, C. J.; Neville, S. M. Guest Programmable Multistep Spin Crossover in a Porous 2-D Hofmann-Type Material. *J. Am. Chem. Soc.* **2017**, *139*, 1330−1335.

(11) Mondal, D. J.; Roy, S.; Yadav, J.; Zeller, M.; Konar, S. Solvent-Induced Reversible Spin-Crossover in a 3D Hofmann-Type Coordination Polymer and Unusual Enhancement of the Lattice Cooperativity at the Desolvated State. *Inorg. Chem.* **2020**, *59*, 13024−13028.
(12) Train, C.; Gheorghe, R.; Krstic, V.; Chamoreau, L. M.; Ovanesyan, N. S.; Rikken, G. L. J. A.; Gruselle, M.; Verdaguer, M. Strong Magneto-Chiral Dichroism in Enantiopure Chiral Ferromagnets. *Nat. Mater.* **2008**, *7*, 729−734.
(13) Clemente-Leon, M.; Coronado, E.; Lopez-Jorda, M.; Desplanches, C.; Asthana, S.; Wang, H.; Letard, J.-F. A hybrid magnet with coexistence of ferromagnetism and photoinduced Fe(III) spin-crossover. *Chem. Sci.* **2011**, *2*, 1121−1127.
(14) Sadakiyo, M.; Ōkawa, H.; Shigematsu, A.; Ohba, M.; Yamada, T.; Kitagawa, H. Promotion of Low-Humidity Proton Conduction by Controlling Hydrophilicity in Layered Metal−Organic Frameworks. *J. Am. Chem. Soc.* **2012**, *134*, 5472−5475.
(15) Abhervé, A.; Clemente-León, M.; Coronado, E.; Gómez-García, C. J.; Verneret, M. One-Dimensional and Two-Dimensional Anilate-Based Magnets with Inserted Spin-Crossover. Complexes. *Inorg. Chem.* **2014**, *53*, 12014−12026.
(16) Sahadevan, S. A.; Abhervé, A.; Monni, N.; Sáenz de Pipaón, C.; Galán-Mascarós, J. R.; Waerenborgh, J. C.; Vieira, B. J. C.; Auban-Senzier, P.; Pillet, S.; Bendeif, E. E.; Alemany, P.; Canadell, E.; Mercuri, M. L.; Avarvari, N. Conducting Anilate-Based Mixed-Valence Fe(II)Fe(III) Coordination Polymer: Small-Polaron Hopping Model for Oxalate-Type Fe(II)Fe(III) 2D Networks. *J. Am. Chem. Soc.* **2018**, *140*, 12611−12621.
(17) Taniguchi, K.; Chen, J.; Sekine, Y.; Miyasaka, H. Magnetic Phase Switching in a Tetraoxolene-Bridged Honeycomb Ferrimagnet Using a Lithium Ion Battery System. *Chem. Mater.* **2017**, *29*, 10053−10059.
(18) Sekine, Y.; Chen, J.; Eguchi, N.; Miyasaka, H. Fine tuning of intra-lattice electron transfers through site doping in tetraoxolene-bridged iron honeycomb layers. *Chem. Commun.* **2020**, *56*, 10867−10870.
(19) Abellán, G.; Martí-Gastaldo, C.; Ribera, A.; Coronado, E. Hybrid Materials Based on Magnetic Layered Double Hydroxides: A Molecular Perspective. *Acc. Chem. Res.* **2015**, *48*, 1601−1611.
(20) Evrard, Q.; Chaker, Z.; Roger, M.; Sevrain, C. M.; Delahaye, E.; Gallart, M.; Gilliot, P.; Leuvrey, C.; Rueff, J. M.; Rabu, P.; Massobrio, C.; Boero, M.; Pautrat, A.; Jaffrès, P. A.; Ori, G.; Rogez, G. Layered Simple Hydroxides Functionalized by Fluorene-Phosphonic Acids: Synthesis, Interface Theoretical Insights, and Magnetoelectric Effect. *Adv. Funct. Mater.* **2017**, *27*, 1703576.
(21) Wellm, C.; Majcher-Fitas, A. M.; Rams, M.; Näther, C. Impact of the Synthetic Approach on the Magnetic Properties and Homogeneity of Mixed Crystals of Tunable Layered Ferromagnetic Coordination Polymers. *Dalton Trans.* **2020**, *49*, 16707−16714.
(22) Pedersen, K. S.; Perlepe, P.; Aubrey, M. L.; Woodruff, D. N.; Reyes-Lillo, S. E.; Reinholdt, A.; Voigt, L.; Li, Z.; Borup, K.; Rouzières, M.; et al. Formation of the Layered Conductive Magnet $CrCl_2(pyrazine)_2$ Through Redox-Active Coordination Chemistry. *Nat. Chem.* **2018**, *10*, 1056−1061.
(23) Perlepe, P.; Oyarzabal, I.; Mailman, A.; Yquel, M.; Platunov, M.; Dovgaliuk, I.; Rouzières, M.; Négrier, P.; Mondieig, D.; Suturina, E. A.; Dourges, M.-A.; Bonhommeau, S.; Musgrave, R. A.; Pedersen, K. S.; Chernyshov, D.; Wilhelm, F.; Rogalev, A.; Mathonière, C.; Clérac, R. Metal-Organic Magnets with Large Coercivity and Ordering Temperatures up to 242°C. *Science* **2020**, *370*, 587−592.
(24) Chorazy, S.; Zakrzewski, J. J.; Magott, M.; Korzeniak, T.; Nowicka, B.; Pinkowicz, D.; Podgajny, R.; Sieklucka, B. Octacyanidometallates for Multifunctional Molecule-Based Materials. *Chem. Soc. Rev.* **2020**, *49*, 5945−6001.
(25) Pinkowicz, D.; Rams, M.; Nitek, W.; Czarnecki, B.; Sieklucka, B. Evidence for Magnetic Anisotropy of $[Nb^{IV}(CN)_8]^{4-}$ in a Pillared-Layered Mn_2Nb Framework Showing Spin-Flop Transition. *Chem. Commun.* **2012**, *48*, 8323−8325.
(26) Nakabayashi, K.; Chorazy, S.; Takahashi, D.; Kinoshita, T.; Sieklucka, B.; Ohkoshi, S. Cesium Cyano-Bridged CoII−MV (M = Mo and W) Layered Frameworks Exhibiting High Thermal Durability and Metamagnetism. *Cryst. Growth Des.* **2014**, *14*, 6093−6100.
(27) Chorazy, S.; Arczynski, M.; Nakabayashi, K.; Sieklucka, B.; Ohkoshi, S. Visible to Near-Infrared Emission from Ln^{III}(Bis-oxazoline)−$[Mo^{V}(CN)_8]$ (Ln = Ce−Yb) Magnetic Coordination Polymers Showing Unusual Lanthanide-Dependent Sliding of Cyanido-Bridged Layers. *Inorg. Chem.* **2015**, *54* (10), 4724−4736.
(28) Nowicka, B.; Bałanda, M.; Gaweł, B.; Ćwiak, G.; Budziak, A.; Łasocha, W.; Sieklucka, B. Microporous $\{[Ni(cyclam)]_3[W(CN)_8]_2\}_n$ Affording Reversible Structural and Magnetic Conversions. *Dalton Trans.* **2011**, *40*, 3067−3073.
(29) Nowicka, B.; Reczyński, M.; Rams, M.; Nitek, W.; Kozieł, M.; Sieklucka, B. Larger Pores and Higher T_c: $\{[Ni(cyclam)]_3[W(CN)_8]_2\cdot solv\}_n$ − a New Member of the Largest Family of Pseudo-Polymorphic Isomers Among Octacyanometallate-Based Assemblies. *CrystEngComm* **2015**, *17*, 3526−3532.
(30) Arimoto, Y.; Ohkoshi, S.; Zhong, Z. J.; Seino, H.; Mizobe, Y.; Hashimoto, K. Photoinduced Magnetization in a Two-Dimensional Cobalt Octacyanotungstate. *J. Am. Chem. Soc.* **2003**, *125*, 9240−9241.
(31) Ohkoshi, S.; Hamada, Y.; Matsuda, T.; Tsunobuchi, Y.; Tokoro, H. Crystal Structure, Charge-Transfer-Induced Spin Transition, and Photoreversible Magnetism in a Cyano-Bridged Cobalt−Tungstate Bimetallic Assembly. *Chem. Mater.* **2008**, *20*, 3048−3054.
(32) Ozaki, N.; Tokoro, H.; Hamada, Y.; Namai, A.; Matsuda, T.; Kaneko, S.; Ohkoshi, S. Photoinduced Magnetization with a High Curie Temperature and a Large Coercive Field in a Co-W Bimetallic Assembly. *Adv. Funct. Mater.* **2012**, *22*, 2089−2093.
(33) Chorazy, S.; Charytanowicz, T.; Pinkowicz, D.; Wang, J.; Nakabayashi, K.; Klimke, S.; Renz, F.; Ohkoshi, S.; Sieklucka, B. Octacyanidorhenate(V) Ion as an Efficient Linker for Hysteretic Two-Step Iron(II) Spin Crossover Switchable by Temperature, Light, and Pressure. *Angew. Chem., Int. Ed.* **2020**, *59*, 15741−15749.
(34) Yoshida, T.; Nakabayashi, K.; Tokoro, H.; Yoshikiyo, M.; Namai, A.; Imoto, K.; Chiba, K.; Ohkoshi, S. Extremely Low-Frequency Phonon Material and its Temperature- and Photo-Induced Switching Effects. *Chem. Sci.* **2020**, *11*, 8989−8998.
(35) Okubo, M.; Kagesawa, K.; Mizuno, Y.; Asakura, D.; Hosono, E.; Kudo, T.; Zhou, H.; Fujii, K.; Uekusa, H.; Nishimura, S.; Yamada, A.; Okazawa, A.; Kojima, N. Reversible Solid State Redox of an Octacyanometallate-Bridged Coordination Polymer by Electrochemical Ion Insertion/Extraction. *Inorg. Chem.* **2013**, *52*, 3772−3779.
(36) Long, J.; Asakura, D.; Okubo, M.; Yamada, A.; Guari, Y.; Larionova, J. Electrochemical Li-Ion Intercalation in Octacyanotungstate-Bridged Coordination Polymer with Evidence of Three Magnetic Regimes. *Inorg. Chem.* **2016**, *55*, 7637−7646.
(37) Reczyński, M.; Heczko, M.; Kozieł, M.; Ohkoshi, S.; Sieklucka, B.; Nowicka, B. Proton-Conducting Humidity-Sensitive Ni^{II}-Nb^{IV} Magnetic Coordination Network. *Inorg. Chem.* **2019**, *58*, 15812−15823.
(38) Imoto, K.; Nakagawa, K.; Miyahara, H.; Ohkoshi, S. Super-Ionic Conductive Magnet Based on a Cyano-Bridged Mn−Nb Bimetal Assembly. *Cryst. Growth Des.* **2013**, *13*, 4673−4677.
(39) Podgajny, R.; Korzeniak, T.; Bałanda, M.; Wasiutyński, T.; Errington, W.; Kemp, T. J.; Alcock, N. W.; Sieklucka, B. 2-D Soft Ferromagnet Based on $[W^{V}(CN)_8]^{3-}$ and Cu^{II} with a T_c of 34 K. *Chem. Commun.* **2002**, 1138−1139.
(40) Korzeniak, T.; Podgajny, R.; Alcock, N. W.; Lewiński, K.; Bałanda, M.; Wasiutyński, T.; Sieklucka, B. A New Family of Magnetic 2-D Coordination Polymers Based on $[M^{V}(CN)_8]^{3-}$ (M = Mo, W) and pre-programmed Cu^{2+} centres. *Polyhedron* **2003**, *22*, 2183−2190.
(41) Kaneko, S.; Tsunobuchi, Y.; Sakurai, S.; Ohkoshi, S. Two-Dimensional Metamagnet Composed of a Cesium Copper Octacyanotungstate. *Chem. Phys. Lett.* **2007**, *446*, 292−296.
(42) Stefańczyk, O.; Majcher, A. M.; Rams, M.; Nitek, W.; Kozieł, M.; Łasocha, W.; Sieklucka, B. Incorporation of Guanidinium Ions in

https://doi.org/10.1021/acs.inorgchem.1c00432
Inorg. Chem. 2021, 60, 10186−10198

Cu^{II}-$[M^{V}(CN)_8]^{3-}$ Double-Layered Magnetic Systems. *Dalton Trans.* **2013**, *42*, 5042−5046.
(43) Podgajny, R.; Chmel, N. P.; Bałanda, M.; Tracz, P.; Gaweł, B.; Zając, D.; Sikora, M.; Kapusta, C.; Łasocha, W.; Wasiutyński, T.; Sieklucka, B. Exploring the Formation of 3D Ferromagnetic Cyano-Bridged $Cu^{II}_{2+x}\{Cu^{II}_4[W^{V}(CN)_8]_{4-2x}[W^{IV}(CN)_8]_{2x}\}\cdot yH_2O$ Networks. *J. Mater. Chem.* **2007**, *17*, 3308−3314.
(44) Ohkoshi, S.; Tokoro, H.; Hozumi, T.; Zhang, Y.; Hashimoto, K.; Mathoniere, C.; Bord, I.; Rombaut, G.; Verelst, M.; Cartier Dit Moulin, C.; Villain, F. Photoinduced Magnetization in Copper Octacyanomolybdate. *J. Am. Chem. Soc.* **2006**, *128*, 270−277.
(45) Wang, T. W.; Wang, J.; Ohkoshi, S.; Song, Y.; You, X. Z. Manganese(II)-Octacyanometallate(V) Bimetallic Ferrimagnets with Tc from 41 to 53 K Obtained in Acidic Media. *Inorg. Chem.* **2010**, *49*, 7756−7763.
(46) Stefańczyk, O.; Podgajny, R.; Korzeniak, T.; Rams, M.; Kozieł, M.; Łasocha, W.; Zając, D. A.; Sieklucka, B. X-ray Absorption Spectroscopy Study of Novel Inorganic−organic Hybrid Ferromagnetic Cu−pyz−$[M(CN)_8]^{3-}$ Assemblies. *Inorg. Chem.* **2012**, *51*, 11722−11729.
(47) Casanova, D.; Cirera, J.; Llunell, M.; Alemany, P.; Avnir, D.; Alvarez, S. Minimal Distortion Pathways in Polyhedral Rearrangements. *J. Am. Chem. Soc.* **2004**, *126*, 1755−1763.
(48) Konieczny, P.; Pełka, R.; Czernia, D.; Podgajny, R. Rotating Magnetocaloric Effect in an Anisotropic Two-Dimensional $Cu^{II}[W^{V}(CN)_8]^{3-}$ Molecular Magnet with Topological Phase Transition: Experiment and Theory. *Inorg. Chem.* **2017**, *56*, 11971−11980.
(49) Gillingham, D.; Geigle, S.; Anatole von Lilienfeld, O. Properties and Reactivity of Nucleic Acids Relevant to Epigenomics, Transcriptomics, and Therapeutics. *Chem. Soc. Rev.* **2016**, *45*, 2637−2655.
(50) Mayoral, M. J.; Bilbao, N.; Gonzalez-Rodriguez, D. Hydrogen-Bonded Macrocyclic Supramolecular Systems in Solution and on Surfaces. *ChemistryOpen* **2016**, *5*, 10−32.
(51) Mayoral, M. J.; Camacho-García, J.; Magdalena-Estirado, E.; Blanco-Lomas, M.; Fadaei, E.; Montoro-García, C.; Serrano-Molina, D.; González-Rodríguez, D. Dye-Conjugated Complementary Lipophilic Nucleosides as Useful Probes to Study Association Processes by Fluorescence Resonance Energy Transfer. *Org. Biomol. Chem.* **2017**, *15*, 7558−7565.
(52) Nakaya, M.; Ohtani, R.; Sugimoto, K.; Nakamura, M.; Lindoy, L. F.; Hayami, S. Molecular Assemblies of Metal Complexes via Base-Pairing of Nucleic Acids in the Crystalline State. *Chem. - Eur. J.* **2017**, *23*, 7232−7237.
(53) Matoga, D.; Szklarzewicz, J.; Mikuriya, M. $[PPh_4]_3[W(CN)_7(O_2)]\cdot 4H_2O$ as the Representative of the $[M(L)_7(LL)]$ Class for Nine-Coordinate Complexes. *Inorg. Chem.* **2006**, *45*, 7100−7104.
(54) Mueller, U.; Förster, R.; Hellmig, M.; Huschmann, F. U.; Kastner, A.; Malecki, P.; Pühringer, S.; Röwer, M.; Sparta, K.; Steffien, M.; et al. The macromolecular crystallography beamlines at BESSY II of the Helmholtz-Zentrum Berlin: Current status and perspectives. *Eur. Phys. J. Plus* **2015**, *130*, 141−150.
(55) Kabsch, W. XDS. *Acta Crystallogr., Sect. D: Biol. Crystallogr.* **2010**, *D66*, 125−132.
(56) Krug, M.; Weiss, M. S.; Heinemann, U.; Mueller, U. XDSAPP: a Graphical User Interface for the Convenient Processing of Diffraction Data Using XDS. *J. Appl. Crystallogr.* **2012**, *45*, 568−572.
(57) *CrysAlis RED and CrysAlis CCD*; Oxford Diffraction Ltd.: Abingdon, Oxfordshire, England, 2000.
(58) Sheldrick, G. M. Crystal structure refinement with SHELXL. *Acta Crystallogr., Sect. C: Struct. Chem.* **2015**, *C71*, 3−8.
(59) Farrugia, L. J. WinGX suite for small-molecule single-crystal crystallography. *J. Appl. Crystallogr.* **1999**, *32*, 837−838.
(60) Altomare, A.; Cuocci, C.; Giacovazzo, C.; Moliterni, A.; Rizzi, R.; Corriero, N.; Falcicchio, A. EXPO2013: a Kit of Tools for Phasing Crystal Structures from Powder Data. *J. Appl. Crystallogr.* **2013**, *46*, 1231−1235.
(61) Favre-Nicolin, V.; Černý, R. 'Free Objects for Crystallography': a Modular Approach to Ab Initio Structure Determination from Powder Diffraction. *J. Appl. Crystallogr.* **2002**, *35*, 734−743.
(62) Petricek, V.; Dusek, M.; Palatinus, L. Crystallographic Computing System JANA2006: General features. *Z. Kristallogr. - Cryst. Mater.* **2014**, *229* (5), 345−352.
(63) Groom, C. R.; Bruno, I. J.; Lightfoot, M. P.; Ward, S. C. The Cambridge Structural Database. *Acta Crystallogr., Sect. B: Struct. Sci., Cryst. Eng. Mater.* **2016**, *B72*, 171−179.
(64) Macrae, C. F.; Bruno, I. J.; Chisholm, J. A.; Edgington, P. R.; McCabe, P.; Pidcock, E.; Rodriguez-Monge, L.; Taylor, R.; van de Streek, J.; Wood, P. A. Mercury CSD 2.0 - new features for the visualization and investigation of crystal structures. *J. Appl. Crystallogr.* **2008**, *41*, 466−470.
(65) Sridhar, B.; Ravikumar, K.; Varghese, B. Supramolecular Hydrogen-Bonded Networks in Adeninediium Hemioxalate Chloride and Adeninium Semioxalate Hemi(oxalic acid) Monohydrate. *Acta Crystallogr., Sect. C: Cryst. Struct. Commun.* **2009**, *C65*, o202−o206.
(66) Hingerty, B. E.; Einstein, J. R.; Wei, C. H. Structure of bisadeninium dinitrate monohydrate, $(C_5H_6N_5^{+}\cdot NO^{3-})_2\cdot H_2O$. *Acta Crystallogr., Sect. B: Struct. Crystallogr. Cryst. Chem.* **1981**, *B37*, 140−147.
(67) Langer, V.; Huml, K. The crystal and molecular structure of adeninium sulphate, $C_5H_5N_5\cdot H_2SO_4$. *Acta Crystallogr., Sect. B: Struct. Crystallogr. Cryst. Chem.* **1978**, *B34*, 1157−1163.
(68) Christensen, J. J.; Rytting, J. H.; Izatt, R. M. Thermodynamic pK, AH0, AS0, and ACP° Values for Proton Dissociation from Several Purines and Their Nucleosides in Aqueous Solution. *Biochemistry* **1970**, *9*, 4907−4913.
(69) Turecček, F.; Chen, X. Protonated Adenine: Tautomers, Solvated Clusters, and Dissociation Mechanisms. *J. Am. Soc. Mass Spectrom.* **2005**, *16*, 1713−1726.
(70) Pasquali, S.; Frezza, E.; Barroso da Silva, F. L. Coars-Grained Dynamic RNA Titration Simulations. *Interface Focus* **2019**, *9*, 20180066.
(71) Bałanda, M.; Pełka, R.; Wasiutyński, T.; Rams, M.; Nakazawa, Y.; Miyazaki, Y.; Sorai, M.; Podgajny, R.; Korzeniak, T.; Sieklucka, B. Magnetic Ordering in the Double-Layered Molecular Magnet Cu(tetren)[W(CN)8]: Single Crystal Study. *Phys. Rev. B: Condens. Matter Mater. Phys.* **2008**, *78*, 174409.
(72) Fahnle, M.; Souletie, J. Exponents far from T_c-a reanalysis of the high-temperature susceptibility of some model systems. *J. Phys. C: Solid State Phys.* **1984**, *C17*, L469.
(73) Carré, E.; Souletie, J. Linear and nonlinear susceptibilities and scaling far from Tc in nickel. *J. Magn. Magn. Mater.* **1988**, *72*, 29−34.
(74) Paulsen, C.; Souletie, J.; Rey, P. Critical Scaling in a Pure Organic Ferromagnet. *J. Magn. Magn. Mater.* **2001**, *226−230*, 1964−1966.
(75) Drillon, M.; Panissod, P.; Rabu, P.; Souletie, J.; Ksenofontov, V.; Gutlich, P. Pressure Effect on the Magnetism of Layered Cooper(II) Compounds with Interlayer Spacing up to 40.7 Å: Nature of the Magnetic Ordering. *Phys. Rev. B: Condens. Matter Mater. Phys.* **2002**, *65*, 104404.
(76) Gupta, R.; DeLapp, J.; Batrouni, G. G.; Fox, G. C.; Baillie, C. F.; Apostolakis, J. Phase Transition in the 2D XY Model. *Phys. Rev. Lett.* **1988**, *61*, 1996.
(77) Cuccoli, A.; Tognetti, V.; Vaia, R. Two-Dimensional XXZ Model on a Square Lattice: A Monte Carlo Simulation. *Phys. Rev. B: Condens. Matter Mater. Phys.* **1995**, *52*, 10221.
(78) Souletie, J.; Rabu, P.; Drillon, M. *Magnetism: Molecules to Materials V*; Miller, J. S., Drillon, M., Eds.; Wiley-VCH, Weinheim, 2005; pp 351.
(79) Berezinsky, V. L. Destruction of Long Range Order in One-Dimensional and Two-Dimensional Systems having a Continuous Symmetry Group. I. Classical systems. *Zh. Eksp. Teor. Fiz.* **1970**, *59*, 907−920.
(80) Kosterlitz, J. M.; Thouless, D. J. Ordering, Metastability and Phase Transitions in Two-Dimensional Systems. *J. Phys. C: Solid State Phys.* **1973**, *6*, 1181.

https://doi.org/10.1021/acs.inorgchem.1c00432
Inorg. Chem. 2021, 60, 10186−10198

(81) Kosterlitz, J. M. The Critical Properties of the Two-Dimensional xy Model. *J. Phys. C: Solid State Phys.* **1974**, *7*, 1046.
(82) Ayed, M.; Mestiri, I.; Ayed, B.; Haddad, A. Synthesis and Characterization of Two Novel Inorganic/Organic Hybrid Materials Based on Polyoxomolybdate Clusters: $(C_5H_5N_5)_2(C_5H_6N_5)_4[(HAsO_4)_2Mo_6O_{18}]\cdot 11H_2O$ and $Na_2(Himi)_3[SeMo_6O_{21}(CH_3COO)_3]\cdot 6H_2O$. *J. Mol. Struct.* **2017**, *1128*, 368−377.
(83) Thabet, S.; Ayed, B.; Haddad, A. A Novel Organic-Inorganic Hybrid Based on Anderson-Type Polyoxometalate: $H\text{-}(C_5N_5H_5)_2(C_5N_5H_6)_2[Al(OH_6)Mo_6O_{18}]\cdot 10H_2O$. *Bull. Mater. Sci.* **2014**, *37*, 1503−1508.
(84) Mito, M.; Iriguchi, K.; Deguchi, H.; Kishine, J.; Kikuchi, K.; Ohsumi, H.; Yoshida, Y.; Inoue, K. Giant nonlinear magnetic response in a molecule-based magnet. *Phys. Rev. B: Condens. Matter Mater. Phys.* **2009**, *79*, 012406.
(85) Atzori, M.; Breslavetz, I.; Paillot, K.; Inoue, K.; Rikken, G. L. J. A.; Train, C. A Chiral Prussian Blue Analogue Pushes Magneto-Chiral Dichroism Limit. *J. Am. Chem. Soc.* **2019**, *141*, 20022−20025.
(86) Atzori, M.; Santanni, F.; Breslavetz, I.; Paillot, K.; Caneschi, A.; Rikken, G. L. J. A.; Sessoli, R.; Train, C. Magnetic Anisotropy Drives Magnetochiral Dichroism in a Chiral Molecular Helix Probed with Visible Light. *J. Am. Chem. Soc.* **2020**, *142*, 13908−13916.

https://doi.org/10.1021/acs.inorgchem.1c00432
Inorg. Chem. 2021, 60, 10186−10198